Meso-scale FE analyses of textile composite reinforcement deformation based on X-ray computed tomography

N. Naouar, E. Vidal-Sallé, J. Schneider, E. Maire, P. Boisse

N. Naouar et al./Composite Structures 116 (2014) 165–176
https://doi.org/10.1016/j.compstruct.2014.04.026

Meso-scale FE analyses of textile composite reinforcement deformation based on X-ray computed tomography

N. Naouar [a,c], E. Vidal-Sallé [a], J. Schneider [c], E. Maire [b], P. Boisse [a,*]

[a] *Université de Lyon, LaMCoS UMR 5259, INSA-Lyon, 27 av Jean Capelle, F-69621 Villeurbanne, France*
[b] *Université de Lyon, MATEIS UMR 5510, INSA-Lyon, 25 av Jean Capelle, F-69621 Villeurbanne, France*
[c] *SNECMA, Site de Villaroche, Rond Point René Ravaud – Réau, F-77550 Moissy-Cramayel, France*

A B S T R A C T

The simulation at meso-scale of textile composite reinforcement deformation provides important infor- mation. In particular it gives the direction and density of the fibres that condition the permeability of the textile reinforcement and the mechanical properties of the final composite. These meso FE analyses are highly dependent on the quality of the initial geometry of the model. Some softwares have been developed to describe composite reinforcement geometries. The obtained geometries imply simplifica- tion that can disrupts the reinforcement deformation computation. The present paper presents a direct method using computed tomography to determine finite element models based on the real geometry of the textile reinforcement. The FE model is obtained for any specificity or variability of the textile reinforcement. The interpenetration problems are avoided. The determination of the fibre direction at each point of the model is detailed. It is a key point for the quality of the deformation simulation. A comparison between FE models obtained from μCT and from a textile geometrical modeller shows that the description of the variability taken into account by the first one leads to a better result.

1. Introduction

Finite element modelling methods applied to design and manufacturing processes are under investigation as a means of generating a predictive design tool for engineers to use when designing composite parts. A large part of these simulations are performed at the macroscopic scale (the global scale of the composite part) (Fig. 1a). In particular, the simulations of the reinforcement preforming [1–3] and of the resin flow in L.C.M. processes (Liquid Composite Moulding) [4–6] are performed at the macroscale. Nevertheless it is necessary to carry out analyses at lower scales to analyse some phenomena. Some studies are conducted at the scale of the fibre (microscopic scale Fig. 1c) to analyse motion and friction between the fibres [7–9]. At the mesoscopic scale (Fig. 1b) the composite is seen as a set of tows (warp and weft yarns in case of 2D woven reinforcements) with or without resin depending on the type of analysis. For periodic structures, mesoscopic models consider the smallest elementary pattern, which can represent the whole fabric by in-plane translation. That domain is called the representative unit cell (RUC) [10–13]. The mesoscopic analyses allow to compute homogenised properties of the composite [10,12,14], damage initiation and propagation [12,15]. The deformation analysis of a reinforcement RUC (with no resin) during the preforming stage provides the geometry of the yarns when the resin is injected. The simulation of the resin flow within these deformed tows allows to compute the permeability of the reinforcement for different local deformations [16,17]. The deformation of the mesoscale geometry of the reinforcement during manufacturing can also be taken into account in the mechanical behaviour of the composite part [18].

The quality of the result of the meso FE modelling strongly depends on the initial FE mesh, its geometry and the associated data in particular the fibre directions. The geometry can be obtained from textile geometrical modelers such as TexGen or WiseTex [19,20]. Nevertheless they provide a simplified geometry of the reinforcements. Moreover the reinforcement architecture are numerous especially for the 3D fabrics [21,22] and they are not all described by these modelers. Finally some interpenetrations can occur between the yarns defined by the modelers in some configurations. In the present study, the initial geometry of meso-FE analyses is directly achieved from a X-ray Micro Tomography (XRMT) [23–27] also called micro computed tomography (μCT). This fairly recent technics allows detailed, accurate and

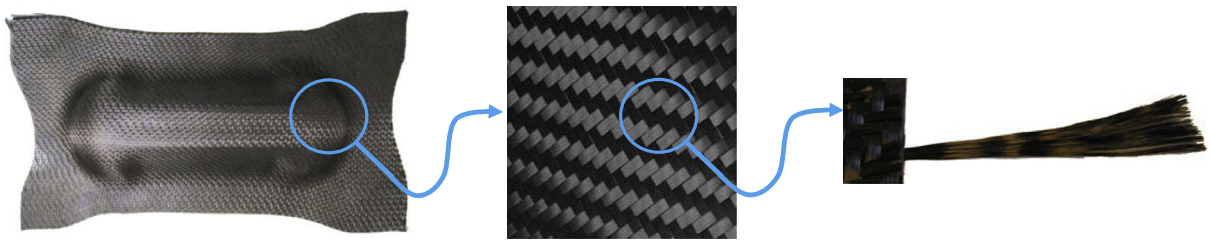

(a) Macroscopic scale (b) Mesoscopic scale (c) Microscopic scale

Fig. 1. Different scales for a woven composite reinforcement.

non-destructive 3D observations inside the material [24]. It allows to distinguish yarns and even fibres defining the anisotropy directions of the material. In the present paper, a methodology is proposed to build automatically finite element models from X-ray micro CT images of the composite or composite reinforcement. These models take into account the specificities of the geometry of the analysed material. They can be obtained for any type of weaving or architecture of the reinforcement. The meso FE modelling of the deformation of a carbon twill weave reinforcement is taken as an example. The determination of the fibre directions within the yarn is a point of main importance. The hypoelastic behaviour used for the FE analysis of the deformation is based on the fibre rotation [28,29]. The meso FE model obtained from μCT images of the carbon twill are used first to identify the parameters of the hypoelastic model of the tow and secondly to simulate biaxial tensile and compaction tests. In the latter case, it is shown that the meso FE model obtained from μCT gives a result closer to experiments than a model built from a textile geometrical modeler.

2. Image processing

2.1. Material and method

The Hexcel G0986® fabric (Fig. 2a) is taken as an example to present the different stages of the method. This fabric is a 2×2 carbon twill weave which characteristics are summarised in Table 1. Images have been acquired using a laboratory tomograph Phoenix V tome X which principles and main functionalities are described in [23–27]. The size of the focus, and thus the resolution is adjustable from 1 to 5 μm. The detector used is made of 1920×1575 pixels each with a size of 127×127 μm. Scans performed in this study used beam values close to 90 keV and 170 μA without additional filter. The trade-off between the resolution and the maximum specimen dimension (i.e. yarn width) allows a maximum resolution of 2 μm. The complete sample must indeed be contained within the cone beam, i.e. in the field of view of the detector. The uncertainty of the measures made by tomography can be estimated to ±1 voxel. Fig. 2b shows the 3D reconstruction by tomography of a G0986 carbon twill reinforcement.

Table 1
Characteristics of G0986 carbon twill.

Characteristics	Values
Weave style	Twill 2/2
Weight distribution warp/weft	50%/50%
Fibres/yarn (warp)	6 K
Fibres/yarn (weft)	6 K
Nominal construction (warp)	3.5 yarns/cm
Nominal construction (weft)	3.5 yarns/cm
Nominal weight	285 g/m^2
Young's modulus (6 K carbon yarn)	228 GPa
Thickness	0.29 mm

2.2. G0986 carbon twill segmentation

The different processes described below are applied successively on each cut of the image stack. The methodology is illustrated for the segmentation of G0986 fabric. Image segmentation consists in partitioning a digital image into multiple segments (sets of pixels). It is sometimes named as superpixeling. In the present case, the goal of segmentation is to separate warp and weft yarns. The first operation consists in obtaining a tomography cut (Fig. 3a) that has undergone an internal treatment by the tomograph software to clean as far as possible the various acquisition artefacts. Orientations of the image are computed thanks to the calculation of the structure tensor [30,31]. This tensor is defined for each pixel as a 2×2 symmetric positive matrix J, where f_x and f_y are the partial spatial derivatives of the image $f(x,y)$, along the principal directions x and y, respectively:

$$J = \begin{bmatrix} \langle f_x, f_x \rangle_w & \langle f_x, f_y \rangle_w \\ \langle f_x, f_y \rangle_w & \langle f_y, f_y \rangle_w \end{bmatrix} \quad (1)$$

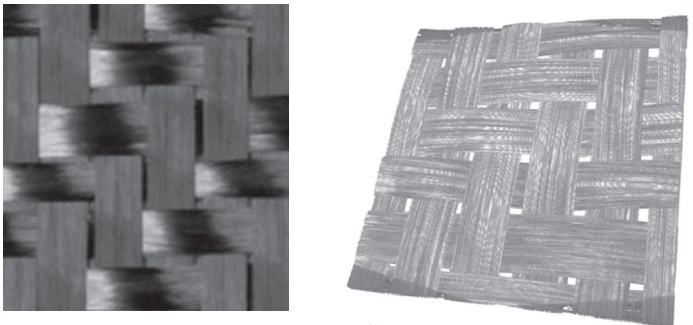

(a) G0986 carbon twill 2/2 (b) G0986 3D reconstruction from μCT

Fig. 2. Hexcel G0986® carbon twill.

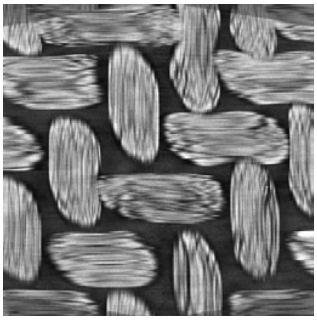

(a) Cut of G0986

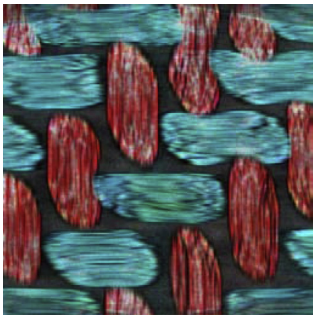

(b) Anisotropy directions

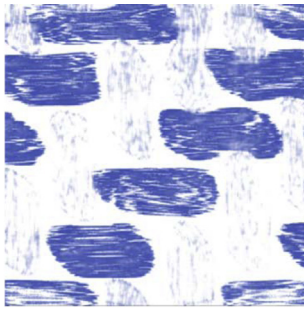

(c) Color deconvolution

(d) Binarization

(e) Median filter

(f) Closing

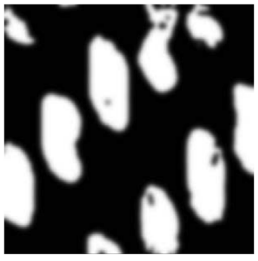

(g) Gaussian blur

(h) Threshold

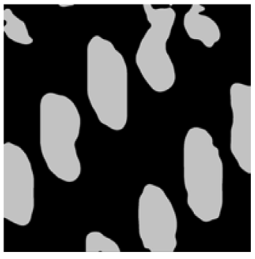

(i) GL assignation

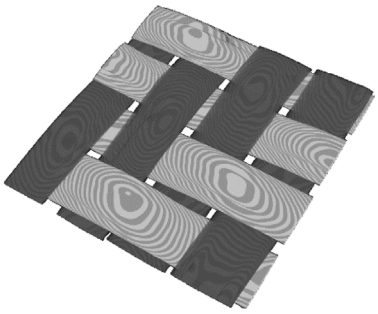

(j) Final result

Fig. 3. Steps of G0986 carbon twill segmentation.

The weighted inner product between two arbitrary images g and h is defined as:

$$\langle g,h\rangle_w = \iint_{R^2} w(x,y)g(x,y)h(x,y)dxdy \quad (2)$$

$w(x,y) \geqslant 0$ is a weighting function that specifies the region of interest (ROI). It is typically a normalised square window of size L that is centered on a location of interest (x_0,y_0). The norm associated with this inner-product is $\|f\|_w = \sqrt{\langle f,f\rangle_w}$.

From this tensor that contains the relevant directional information, three features [32,33] are calculated: the local orientation θ, the energy E and the coherency C. The local predominant orientation θ in the considered region corresponds to the direction of the largest eigenvector of the structure tensor. It is thus given by

$$\theta = \frac{1}{2}\arctan\left(2\frac{\langle f_x,f_y\rangle_w}{\langle f_y,f_y\rangle_w - \langle f_x,f_x\rangle_w}\right) \quad (3)$$

The energy parameter E is defined as the trace of the tensor matrix

$$E = Trace(J) = \langle f_x,f_x\rangle_w + \langle f_y,f_y\rangle_w \quad (4)$$

Pixels with higher energy values correspond to less isotropic and more clearly oriented structures. The coherency parameter C is defined as the ratio between the difference and the sum of the maximum and minimum tensor eigenvalues.

$$C = \frac{\lambda_{max}-\lambda_{min}}{\lambda_{max}+\lambda_{min}} = \frac{\sqrt{(\langle f_y,f_y\rangle_w - \langle f_x,f_x\rangle_w) + 4\langle f_x,f_y\rangle_w}}{\langle f_x,f_x\rangle_w + \langle f_y,f_y\rangle_w} \quad (5)$$

Coherency is bounded between 0 and 1, with 1 indicating highly oriented structures and 0 indicating isotropic areas.

Depending on the orientation θ, each pixel is assigned a colour. Because the textile materials analysed in the present study exhibit two directions of anisotropy in warp and weft direction, the associated orientation map mainly presents two distinct colours (Fig. 3b). A colour deconvolution (Fig. 3c), allows to separate pixels with the same colour and to produce images representing only warp or weft directions.

The next operation of that segmentation is the binarization (Fig. 3d). Such operation produces two classes of pixels: black pixels and white ones. A median filter (Fig. 3e) is firstly used to "clean" the image. Each pixel of the image to be filtered is replaced by the median value of neighbouring pixels. The aim is to get a plain shape representing the yarn. To achieve this objective, a binary closing operation is applied (Fig. 3f), which is made of a dilation followed by an erosion. This technique allows to remove small holes, to preserve the size and shape of the element and to merge elements that are very close. A Gaussian blur filter (Fig. 3g) followed by a threshold (Fig. 3h) allows to get filled yarn sections. Finally, a gray level is assigned (GL) (Fig. 3i) for images in the warp direction and another one for images in the weft direction. Images in the warp and weft directions are then superimposed (Fig. 3j).

2.3. Skeletonisation

Skeletonisation provides a compact representation of the objects even in the case of complex shapes and topologies. In 2D, the skeletons are inter-connected lines in the image centre, as shown in Fig. 4. Skeletons are widely used in image analysis and pattern recognition, since they allow to describe synthetically not only the shapes but also mathematical properties of objects, such as length or surface. They are also used in image compression because they describe the objects in a compact way. Several algorithms have been proposed to compute skeletons [34]. In the present study, the algorithm used is the method developed by Fouard et al. [35]:

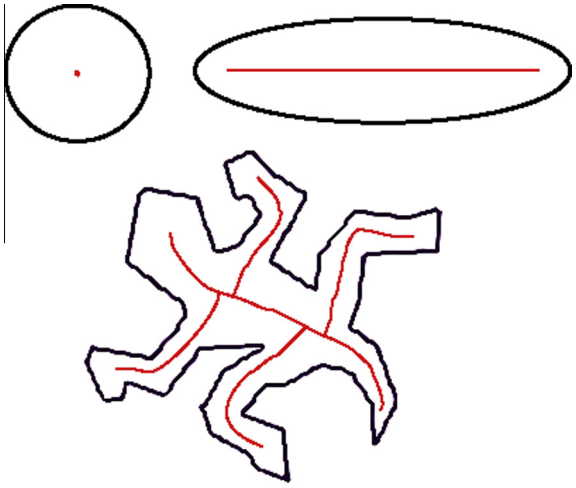

Fig. 4. Skeleton examples.

2.3.1. Definition

A skeleton is a subset of the foreground object that verifies the following properties:

- **Homotopy**: the skeleton is topologically equivalent to the original image. It has the same number of connected components, holes and cavities as the original image.
- **Thinness**: the skeleton is one point wide except at junction points, where the connectivity can require several points.
- **Medialness**: the skeleton is centrally located within the foreground object.

Skeletons can be built in the continuous space using Voronoï diagrams. Discrete points are chosen on the object contour. The skeleton is the subgraph of the Voronoï diagram of these points, which is entirely included within the object. The obtained skeleton is connected, topologically equivalent to the object, centred and thin. But this method rises difficulties when applied in the discrete space.

2.3.2. Skeletonisation discrete methods

The algorithm complexity and the computational time are an encumbrance for heavy images. Discrete methods are generally fast and easy to use. The skeletonisation process can be based on:

- **Thinning**: the skeleton is computed by iteratively peeling off the boundary of the object, layer-by-layer. The deletable points (simple points that are also border points and non-end points) are removed either sequentially [36] or in parallel [37,38], or with morphological operations [39]. These methods lead to a skeleton homotopic to the object, by construction, thin and geometrically representative (if the endpoints have been correctly characterised), but not necessarily centred.
- **Distance maps**: the skeleton is defined as the locus of the local maxima of the distance map [40,41]. The principle of these methods is to calculate the distance map of the object, to find local maxima and to reconnect these maxima. The resulting skeleton is centred by construction, thin, depending on the local maxima threshold, but not necessarily homotopic, depending on the path reconstruction.

Hybrid methods have been recently introduced to take advantage of both of these approaches [42]. These methods, called Distance Ordered Homotopic Thinning (DOHT), use a homotopic thinning, i.e. an iterative deletion of simple points, leading to a

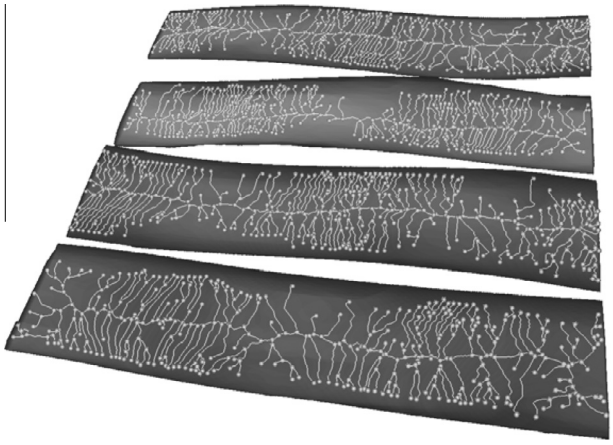

Fig. 5. Skeleton of G0986 carbon twill.

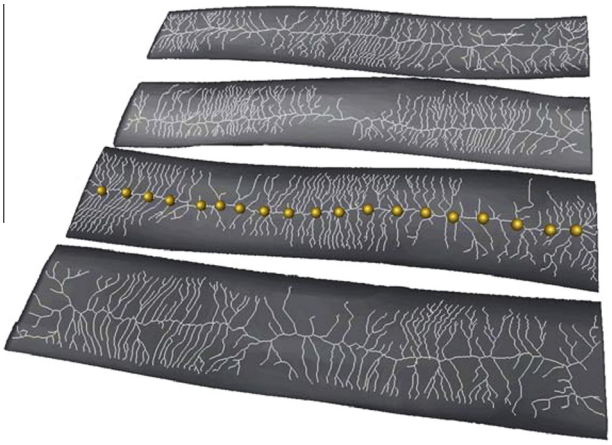

Fig. 7. Spline on neutral axis.

homotopic skeleton, but in the increasing distance map order leading to a centred skeleton.

Applying these technics [35] to composite reinforcement leads to the skeleton shown Fig. 5 from 3D reconstructed reinforcements. This looks like "fishbones".

From this fishbone-like skeleton, it is necessary to recover the "backbone" which represents the neutral axis of each yarn. To achieve this aim, a nodes retrieval algorithm of the "backbone" has been developed. From the voxels coordinates of a yarn, the number of connectivity (number of links of a voxel with its neighbours) greater than one is calculated (Fig. 6a). While the number of connectivity greater than one is superior than the minimal number of connectivity equal to one (number of extremity of each yarn), the algorithm removes the nodes attached to these connectivities (Fig. 6b). Thus, the nodes of the "backbone" are cleaned of their transversal edges (Fig. 6c). The subsequent operation is to construct a B-spline curve through these nodes to get the neutral axis (Fig. 7).

The main objective of the skeletonisation is to provide the material orientation of the yarns. For that, a direction vector is assigned to each node of the spline. In the specific case of yarn modelling, it is assumed that the yarn is characterised by (Fig. 8):

- The middle line where the centre G of the curvilinear abscissa is positioned by $X(s)$.
- Its cross section at the curvilinear abscissa s.
- A local material coordinate system (Frenet–Serret):

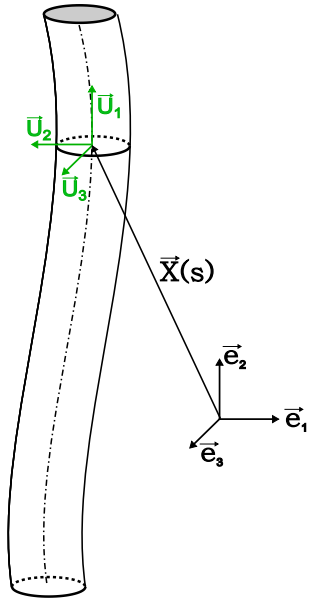

Fig. 8. Yarn geometry.

$$\vec{u}_1 = \frac{d\vec{X}}{ds} = \vec{t} \tag{6}$$

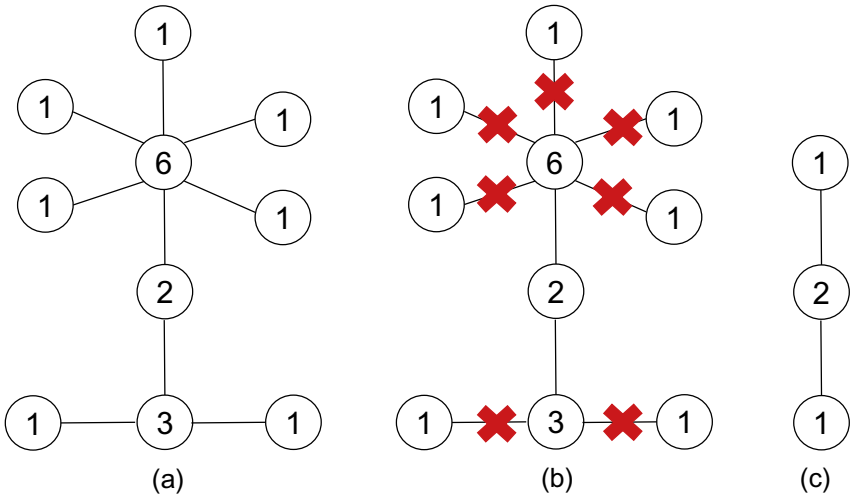

Fig. 6. Scheme of nodes retrieval algorithm of the "backbone".

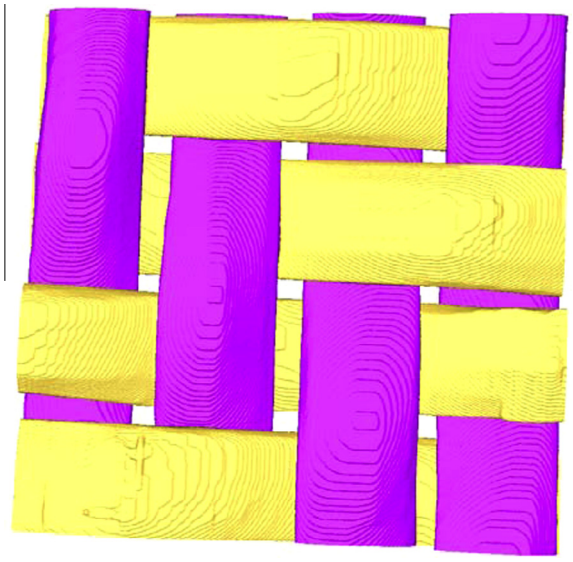

Fig. 9. Labelling of G0986 carbon twill.

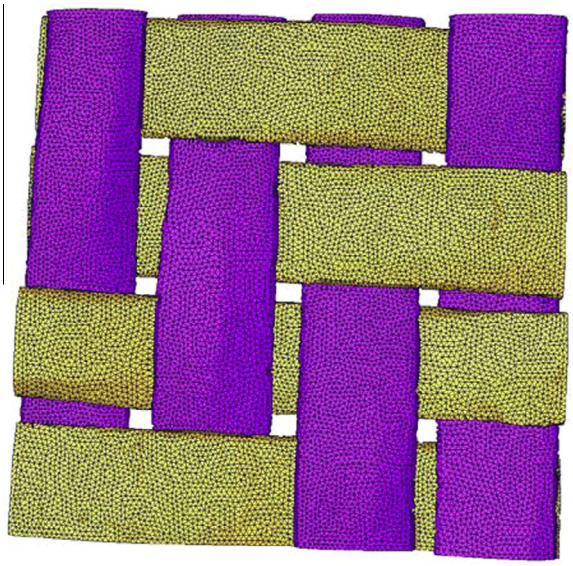

Fig. 10. Mesh of G0986 carbon twill.

$$\vec{u}_2 = \frac{d^2\vec{X}}{ds^2} = \frac{\vec{n}}{\rho} \text{ with } \rho = \frac{1}{\left\|\frac{d\vec{t}}{ds}\right\|} \tag{7}$$

$$\vec{u_3} = \vec{t} \wedge \vec{n} = \vec{b} \tag{8}$$

3. Mesh generation

At mesoscopic scale, the mechanical analysis of composite reinforcements is based on the finite element method. This method relies on subdomains that are defined by a mesh. The mesh generation boils down to building a "triangulation" that precisely catches the domain described in practice by a discretization of its boundary [43]. The aim of the present section is to transform the tomography image into discrete geometry.

3.1. Surface generation

After the segmentation step described in the previous section, a labelling of 3D images is carried out. Voxels that belong to the same gray level are grouped and are assigned a mark. Therefore, it is possible to create a polygonal surface corresponding to the labelled yarns (Fig. 9) by triangularizing the external surface of each phase (i.e. each colour) with triangles using the marching cubes algorithm [44].

3.2. Surface simplification algorithm

The reconstructed surfaces after three-dimensional segmentation generally involve too many triangles. For a reason of computation time, the number of triangles of the reconstructed surfaces must be reduced. This operation is carried out using an algorithm based on the edges contraction. The algorithm developed by Garland and Heckbert [45] simplifies polygonal models rapidly while preserving information. The method relies on successive vertices pair contractions. It guarantees the surface topology with a squared error calculation. By contracting vertices pair, the algorithm can gather disjoint parts of the model. This process is called aggregation.

3.3. Advancing front mesh generation method

After the surface simplification step, a volume mesh generation is carried out from a front algorithm [46,47]. The algorithm starting point is the triangulated surface. The triangles of discretized border form the initial front. From this front, tetrahedra are generated step by step until the centre of the domain is reached (Fig. 10). As a consequence, in the domain centre, tetrahedra quality is poorer than in the external surface due to front collisions. An accurate tuning of the meshing algorithm can avoid such poor quality.

In order to perform a FE calculation, a specific constitutive behaviour is needed. Such behaviour must be based on the local material orientation [28,48]. From the yarn direction obtained by skeletonisation result, each tetrahedral element of the mesh can be oriented. The importance of that point will be focussed later. The yarn is partitioned (Fig. 11) in order to assign local orientations by zones. It is possible to refine the partition by adjusting the spline discretization. Then it is sufficient to assign these local orientations to each element in the same zone. An hypoelastic approach for materials large strains of one fibre direction has been proposed in [28,48]. It is based on the rotation of the fibre that must be strictly followed during the deformation.

4. Simulation and discussion

Fig. 12 shows a X-ray tomography imaging of a textile reinforcement yarn. This yarn is composed of nearly parallel fibres and can be considered as a transversally isotropic material. This has been confirmed by experimental observations [48,49]. In particular, covariance analyses, providing information about the spatial distribution of fibres for different deformations, justify this assumption [48]. When the yarn is considered as a continuous material the main attribute of such a material lies in its strong stiffness in the fibre direction, in comparison to transverse rigidities, so one of the main issues of the constitutive model is the following of the anisotropy direction. This problem lies at the crossroads of two important points: the principle of objectivity on the one hand and updating stress state during the numerical integration on the other hand.

4.1. Hypoelastic law

The proposed model must fullfil the large transformation requirements: the phenomena to be modelled include geometric nonlinearities due to large displacements and large deformations

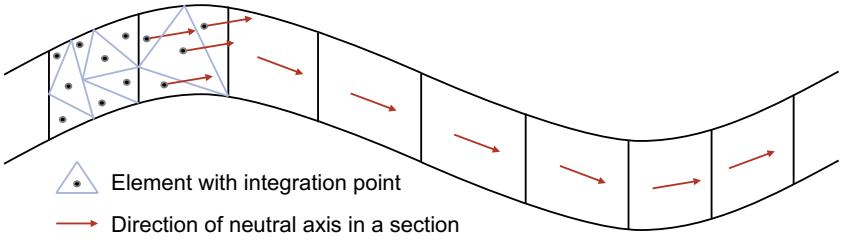

Fig. 11. Yarn partition.

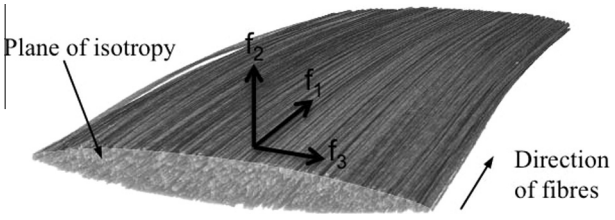

Fig. 12. Transverse isotropy of the yarn in a textile reinforcement. X-ray tomography imaging.

of the yarns. It has been chosen in this study to use a hypoelastic approach. Indeed, the yarns are subjected to large strains and rotations, so that the orientation of the material is significantly modified and the fibre direction has to be strictly followed. The hypoelastic laws or the rate constitutive equations [50–52] can be written as:

$$\underline{\underline{\sigma}}^{\nabla} = \underline{\underline{\underline{\underline{C}}}} : \underline{\underline{D}} \tag{9}$$

where $\underline{\underline{\sigma}}$ and $\underline{\underline{D}}$ are, respectively, the Cauchy stress rate tensor and the strain rate tensor. These two tensors are defined on the current configuration. $\underline{\underline{\sigma}}^{\nabla}$ is an objective time derivative of $\underline{\underline{\sigma}}$. The aim of this derivative is to avoid the part due to rigid body rotations in the time derivative of the Cauchy stress. $\underline{\underline{\sigma}}^{\nabla}$ is a derivative for an observer which is fixed with regard to the material,

$$\underline{\underline{\sigma}}^{\nabla} = \underline{\underline{Q}} \cdot \left(\frac{d}{dt} \left(\underline{\underline{Q}}^{T} \cdot \underline{\underline{\sigma}} \cdot \underline{\underline{Q}} \right) \right) \cdot \underline{\underline{Q}}^{T} \tag{10}$$

where Q is the rotation from the initial orthogonal frame to the so-called rotating frame where the objective derivative is made. There are several objective rates approaching this goal. The Green–Naghdi and Jaumann objective derivatives are the most commonly used in the FE software [53,54]. They are respectively based on the rotation of the polar decomposition of the deformation gradient tensor $\underline{\underline{F}} = \underline{\underline{R}} \cdot \underline{\underline{U}}$, and the rotation of the corotational frame. These are routinely used for analyses of metals at high strains. All of them avoid the stress change under rigid body rotations.

It has been established that both of them are not suitable for fibrous material [28,29]. The longitudinal rigidity is very high in comparison to the transverse behaviour, consequently, the fibre direction has to be strictly followed. The objective derivative, used in this study, was defined by Hagege and Badel [28,29] and is based on the rotation $\underline{\underline{\Phi}}$ from the frame based on the initial directions of the fibres $\underline{e_i^0}$ to the frame of current directions $\underline{f_i}$ (Fig. 12), i ∈ [1,3] where

$$\underline{f_1} = \frac{\underline{\underline{F}} \cdot \underline{e_1^0}}{\left\| \underline{\underline{F}} \cdot \underline{e_1^0} \right\|}, \quad \underline{f_2} = \frac{\underline{\underline{F}} \cdot \underline{e_2^0} - \left(\underline{\underline{F}} \cdot \underline{e_2^0} \cdot \underline{f_1} \right) \underline{f_1}}{\left\| \underline{\underline{F}} \cdot \underline{e_2^0} - \left(\underline{\underline{F}} \cdot \underline{e_2^0} \cdot \underline{f_1} \right) \underline{f_1} \right\|}, \quad \underline{f_3} = \underline{f_1} \times \underline{f_2} \tag{11}$$

Eq. (9) is integrated over a time increment $\Delta t = t^{n+1} - t^n$ using the Hughes and Winget formula widely used in finite element codes at finite strains [52]:

$$[\boldsymbol{\sigma}^{n+1}]_{f_i^{n+1}} = [\boldsymbol{\sigma}^{n}]_{f_i^{n}} + [\mathbf{C}^{n+1/2}]_{f_i^{n+1/2}} [\Delta \boldsymbol{\varepsilon}]_{f_i^{n+1/2}} \tag{12}$$

where $[\Delta \boldsymbol{\varepsilon}]_{f_i^{n+1/2}} = [\mathbf{D}]_{f_i^{n+1/2}} \Delta t$.

In Eq. (12), the constitutive matrix $[C]_{f_i}$ is expressed in the basis $\{\underline{f_i}\}$ based on the fibre orientation at current time (Fig. 12). This is important because the longitudinal behaviour in direction $\underline{f_1}$ and the transverse behaviours in-plane ($\underline{f_2}$, $\underline{f_3}$) are distinguished (see latter).

As previously mentioned, X-ray tomography observations lead to the assumption of a yarn transversely isotropic behaviour. Based on this assumption, the constitutive relation used in this paper is decomposed into two parts. First, the longitudinal direction is considered; and then, the isotropic transverse behaviour is split into a "spherical" and a "deviatoric" part.

4.1.1. Longitudinal behaviour

The importance of a correct follow up of the fibre direction has been already pointed out [48].

The material coefficients of the yarn constitutive tensor are determined from different experimental tests. The longitudinal Young modulus E is known from a tension test on a single yarn. To keep the yarn bending stiffness low enough, the longitudinal shear moduli G_{12} and G_{13} low and assumed to have equal values: $G_{12} = G_{13} = G$. Longitudinal Poisson ratios are assumed to be null.

4.1.2. Transverse behaviour

During the reinforcement deformation, the fibre bundle exhibits both volume and shape changes. Those observations, lead to use a decomposition of the strain tensor. The strain field in the transverse plane is split in a "spherical" part, representative to the area change of the yarn section, and a "deviatoric" part, characterising the shape change of the fibre bundle. Such as:

$$[\varepsilon_T]_{f_i} = \begin{bmatrix} \varepsilon_s & 0 \\ 0 & \varepsilon_s \end{bmatrix} + \begin{bmatrix} \varepsilon_d & \varepsilon_{23} \\ \varepsilon_{23} & -\varepsilon_d \end{bmatrix} \tag{13}$$

with $\varepsilon_s = \frac{\varepsilon_{22}+\varepsilon_{33}}{2}$ et $\varepsilon_d = \frac{\varepsilon_{22}-\varepsilon_{33}}{2}$.

That decomposition is assumed to be also valid for the strain increment and for the stress increment tensors. That leads to the constitutive equation

$$\begin{aligned} \Delta\sigma_s &= A\, \Delta\varepsilon_s \\ \Delta\sigma_d &= B\, \Delta\varepsilon_d \\ \Delta\sigma_{23} &= C\, \Delta\varepsilon_{23} \end{aligned} \tag{14}$$

in which A, B and C are material parameters depending on both longitudinal tensile strain and spherical strain ε_s and identified by an inverse method. Moreover, it can be shown that $B = C$ [48]. $\Delta\sigma_s$, $\Delta\sigma_d$, $\Delta\varepsilon_s$, $\Delta\varepsilon_d$ are respectively spherical and deviatoric stress and

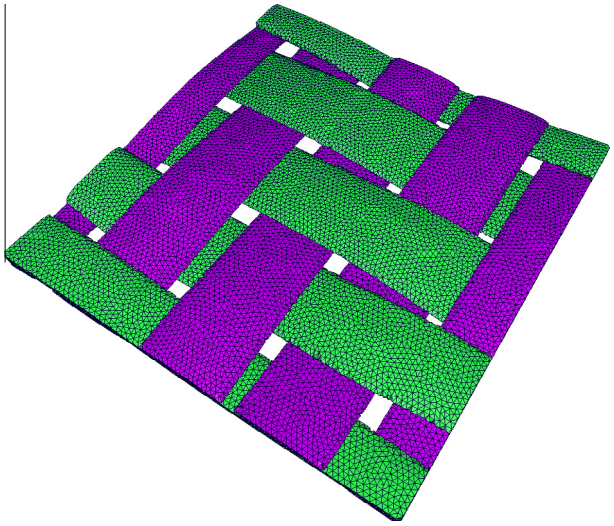

Fig. 13. A meshed representative unit cell of the carbon twill 2/2 fabric with material boundaries.

strain increments. A reasonable experimental fit is found with parameters A and B given by the expressions of equation [48]

$$A = A_0\, e^{-p\varepsilon_s} e^{n\varepsilon_{11}}$$
$$B = B_0\, e^{-p\varepsilon_s} \tag{15}$$

Finally, the constitutive matrix of the material in the fibre directions is in the form

$$[C]_{f_i} = \begin{bmatrix} E & 0 & 0 & 0 & 0 & 0 \\ & \frac{A+B}{2} & \frac{A-B}{2} & 0 & 0 & 0 \\ & & \frac{A+B}{2} & 0 & 0 & 0 \\ & \textit{Symmetry} & & G & 0 & 0 \\ & & & & B & 0 \\ & & & & & G \end{bmatrix} \tag{16}$$

4.2. Periodic boundary conditions

The periodicity of the reinforcement is used to set the size of the geometric model. The smallest geometry to be modelled is that of a representative unit cell of the reinforcement, i.e. the smallest pattern allowing the reconstruction of the whole fabric by translations only. Its choice is not unique. Nevertheless, the choice of a unit cell with fibres (and not void) on the boundaries is preferred in the present study (Fig. 13) because it is possible to prescribe boundaries conditions on the complete frontier. The periodicity of the reinforcement must be guaranteed during the test, which is achieved through appropriate boundary conditions. The displacement field is of the form [11,13]:

$$\underline{\varphi}(\underline{X}) = \underline{\varphi_m}(\underline{X}) + \underline{w}(\underline{X}) \tag{17}$$

with $\underline{\varphi_m}$ denoting the macroscopic displacement field, and $\underline{w}$ the periodic local displacement field. Then periodicity implies

$$\underline{w}(\underline{X_\alpha^-}) = \underline{w}(\underline{X_\alpha^+})\ (\alpha = 1 \text{ or } 2) \tag{18}$$

where $\underline{X_\alpha^-}$ and $\underline{X_\alpha^+}$ are paired positions on two opposite boundaries, i.e. they can be deduced by an $\underline{x}$ or $\underline{y}$ translation. As a consequence the corners of the cell must verify $\underline{w} = 0$.

Finally Eqs. (17) and (18) lead to the periodic boundary conditions for two paired points of opposite boundaries:

$$\underline{x_\alpha^-} - \underline{x_\alpha^+} = \underline{\varphi_m}(\underline{X_\alpha^+}) - \underline{\varphi_m}(\underline{X_\alpha^-}) \tag{19}$$

where $\underline{x_\alpha^+}$ and $\underline{x_\alpha^-}$ denote the positions in the deformed configuration. The material constitutive model developed in the previous section is implemented in a user subroutine. The values of the material parameters are given in Table 1. Yarn to yarn contacts are assumed to induce Coulomb friction with a uniform coefficient of 0.24 [56–58]. The calculations have been carried out using 4-nodes continuum tetrahedral elements.

4.3. Simulation results: material parameters identification

Fig. 14 presents the simulation of the tensile biaxial test of a G0986 carbon twill specimen. The warp and weft yarns are both loaded in tension [59]. The cross geometry of the specimen is well adapted to fibre fabrics. Their in-plane shear stiffness is weak in comparison to the tensile rigidity, consequently the biaxial tensile device can prescribe quasi-homogenous strain fields even in the internal corners of the specimen. In Fig. 15, the red square curve represents a tensile experimental test on a single yarn. The tensile curve is linear. The longitudinal Young modulus of the yarn is determined from this test: $E = 116{,}000$ MPa (this value is linked to the initial cross-sectional area used in the finite element model).

The transverse properties A_0, B_0, p, n are determined by an inverse approach based on a Levenberg–Marquardt algorithm [60]. These parameters are calculated from the tensile equibiaxial test with identical strain ratio in warp and weft directions $k = \frac{\varepsilon_{warp}}{\varepsilon_{weft}} = 1$ (k = strain in the warp direction/strain in the weft direction). During this test, the yarns in warp and weft directions are both in tension and submitted to strong transverse compaction [55]. Thus the hypoelastic law coefficients can be identified (Table 2). In this equibiaxial tensile test, the curves are plotted in only one direction because the fabric is quasi balanced. The nonlinearity is due to decrimping and yarn compaction. The stiffness in the transverse direction (direction perpendicular to the fabric)

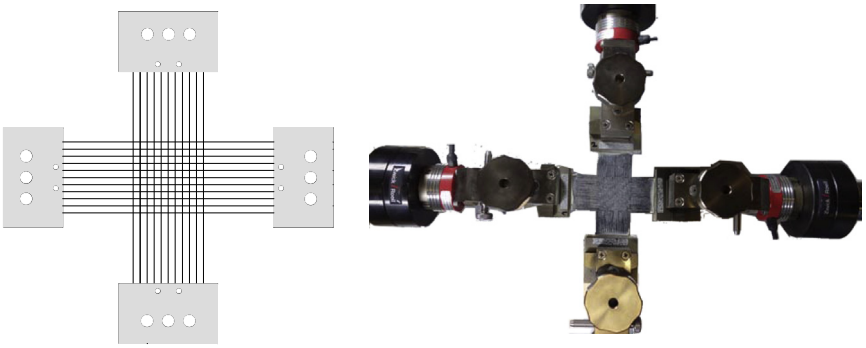

Fig. 14. Cross shaped specimen and biaxial tensile test.

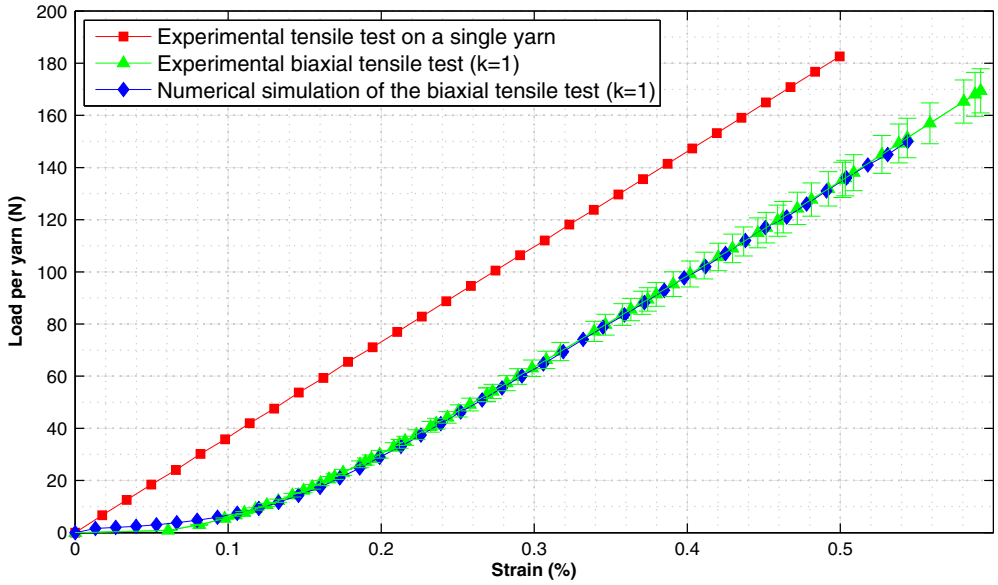

Fig. 15. Tensile test on a single yarn and equibiaxial tensile test simulation ($k = 1$).

Table 2
Parameters of the hypoelastic law of the carbon yarns of the G0986 carbon twill.

E	A_0	B_0	p	n
116,000 MPa	3.73858	10.3798	−0.00111002	2.1905

is weak at the beginning of the loading and increases strongly with compaction [61,62].

4.4. Validation in biaxial tension

Using the material parameters identified in Section 4.3 (and listed in Table 2), the biaxial tensile tests are simulated with the FE model built from μCT for different ratio k and compared to experiments (Fig. 16). The response depends on the ratio k. In particular, the initial non-linearity decreases when k increases. A good agreement is obtained between the simulated curves and the experimental curves. The green triangle curve in Fig. 16 is a unidirectional tensile test on the G0986 fabric. In this test the yarns in the direction perpendicular to the tension are free (no prescribed displacements). The non-linearity of the tensile behaviour is maximum. The loaded yarns become straight. Here again the simulation based on the FE model built from μCT is in good agreement with the experiment.

4.5. Validation in transverse compaction

Fig. 18 shows the results of a transverse compaction test on the G0986 carbon twill. The material parameters used in the simulation are those identified in Section 4.3 (Table 2). The simulation is performed on a representative unit cell (RUC) (Fig. 17) on which periodic boundary conditions have been prescribed. The behaviour is non-linear and the transverse stress follows a "J" shape when increasing the fibre volume fraction V_f where

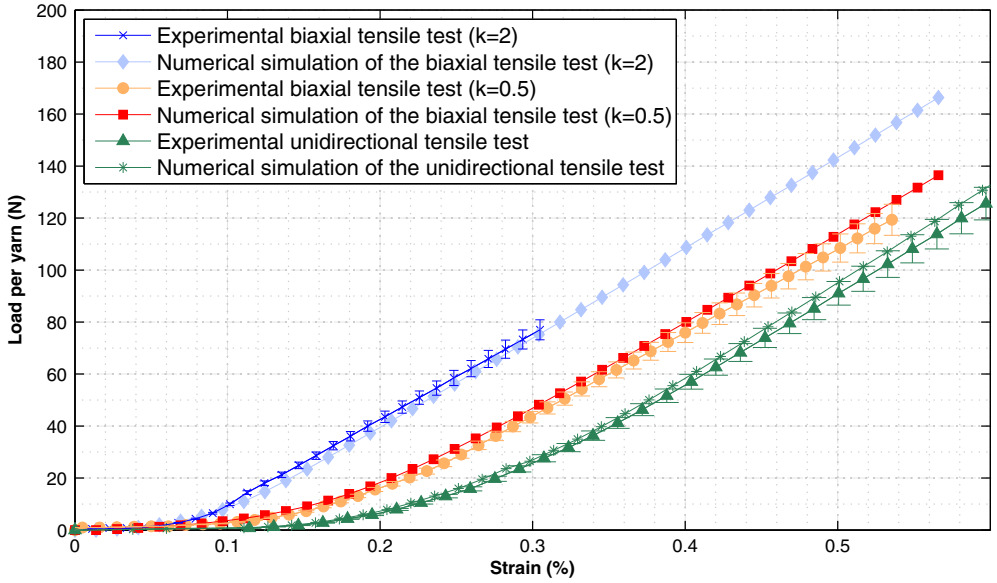

Fig. 16. Biaxial tests for different k.

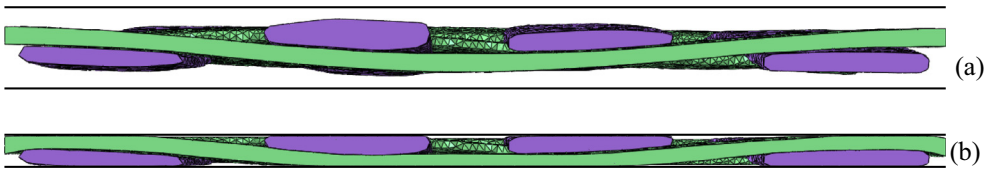

Fig. 17. Simulation of G0986 carbon twill. (a) Geometry before compaction (b) after compaction.

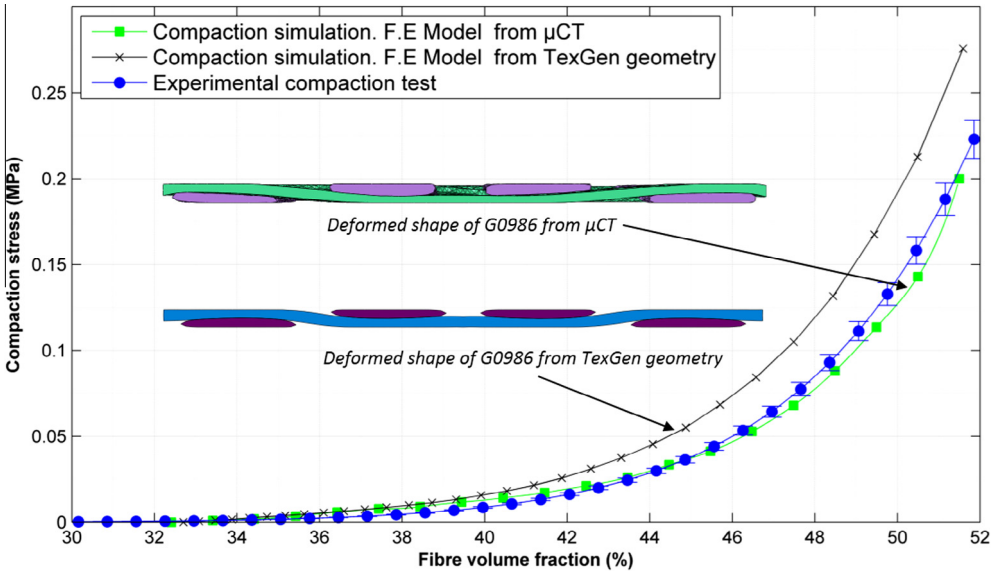

Fig. 18. Compaction test: simulations and experiment.

$$V_f = \frac{V_{fibre}}{V_{sample}} = \frac{m_s S_{sample}}{\rho S_{sample} \delta} = \frac{m_s}{\rho \delta} \tag{20}$$

- m_s : areal mass of the fabric.
- ρ: density of the reinforcement.
- δ : fabric thickness (decreases during the test).

At the beginning of the test when applied forces are low, the thickness of the reinforcement decreases mainly due to the closure of the pores between the fibres and the loss of undulation of the yarns (Fig 17). As this stage is dominated by the bending behaviour of fibres, the volume fraction of fibres increases quickly with pressure. Then the fibres are laterally in contact and the load increases strongly [61,62]. The load obtained from the meso FE model built from μCT and from the compaction experiment in Fig. 18 are in good agreement.

4.6. Comparison with a compaction simulation based on a textile geometrical modeller

The simulation of the compaction test on the G0986 carbon twill is performed from a geometrical model obtained with the TexGen software developed at the University of Nottingham as a modelling pre-processor for textiles [19,63,64]. The TexGen geometrical model is shown on Fig. 19c. The version 3.6.1 of TexGen has been used [65]. Interpenetrations are avoided in the G0986

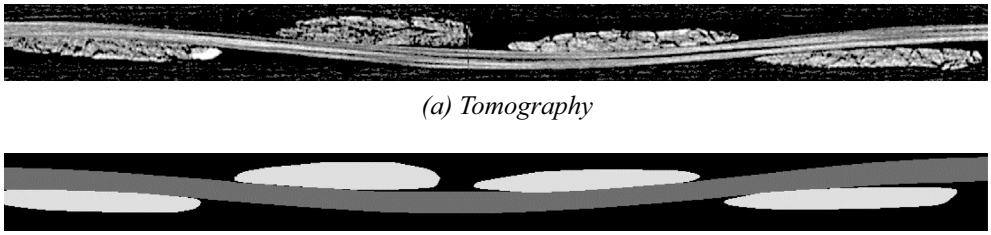

(a) Tomography

(b) Geometry obtained by the method presented in the present paper

(c) TexGen model

Fig. 19. Slices in G0986 warp plane.

carbon twill model. This TexGen model is compared in Fig. 19 to the tomography slice and to the geometry obtained from this tomography by the method described in Section 2. Differences can be noticed. The TexGen model is more regular. The cross sections of the different yarns are identical while those obtained by tomography are slightly different. In addition the contact zones between the different warp and weft yarns varies in the μCT model while they respect the symmetry of the unit cell in the TexGen model. Overall this TexGen model well describes the G0986 twill but does not includes the variability of the specimen that are taken into account in the model built from μCT. These differences has an influence on the mechanical response of the reinforcement.

The two models (TexGen and using computed tomography) are meshed and used to compute the compaction of the G0986 reinforcement. The mechanical properties are the same and have been identified from equibiaxial tensile test (Section 4.3). The results obtained by the 'tomography' model are in good agreement with the experiments (Fig 18). The TexGen model give a more stiff solution. This is due to the idealised geometry that does not include some geometrical imperfections and increase somewhat the rigidity.

5. Conclusions

X-ray Micro Tomography is one possible way to define meso FE models directly from a composite or composite reinforcement specimen. This method can be used for any type of reinforcement and in particular for those that have not be taken into account in textile modellers. The specificities and variability of the reinforcement are taken into account. The different steps to obtain the FE model have been detailed. In particular the definition of the fibre directions is a key point for the mechanical behaviour. The present method main advantages are first to avoid the yarn interpenetrations and secondly to take into account the variability of the reinforcement that generally decreases its rigidities.

The constructed meshes are made of tetrahedrons because it is the shape that is the best-adapted shape for automatic meshing. Tetrahedrons are not always the more efficient elements. It will be necessary to investigate the possibly to obtain hexahedral meshes from micro tomography. The carbon twill taken in the present paper as an example is rather simple. It will be now necessary to obtain meso FE model in the case of complex reinforcements. It is clear that the presented method is particularly interesting when the geometry of the reinforcement is complicated (3D, interlocks...).

Acknowledgements

The collaboration with SNECMA is gratefully acknowledged. This work was supported under the PRC Composites, Research project funded by DGAC, involving SAFRAN Group, ONERA and CNRS.

References

[1] Long AC. Composites forming technologies. In: Long AC, editor. Woodhead publishing series in textiles, vol. 61. 2007.
[2] Boisse P. Composite reinforcements for optimum performance. In: Boisse P, editor. Woodhead publishing series in composites science and engineering, vol. 36. 2011.
[3] Gereke T, Dobrich O, Hubner M, Cherif C. Experimental and computational composite textile reinforcement forming: a review. Compos A: Appl Sci Manuf 2013;46(1):1–10.
[4] Advani SG. In: Advani SG, editor. Flow and rheology in polymeric composites manufacturing. Elsevier Science; 1994.
[5] Correia N, Robitaille F, Long A, Rudd C, Simacek P, Advani SG. Use of resin transfer molding simulation to predict flow, saturation and compaction in the VARTM process. J Fluids Eng 2004;126(2):210–5.
[6] Trochu F, Ruiz E, Achim V, Soukane S. Advanced numerical simulation of liquid composite molding for process analysis and optimization. Compos A: Appl Sci Manuf 2006;37(6):890–902.
[7] Zhou G, Sun X, Wang Y. Multi-chain digital element analysis in textile mechanics. Compos Sci Technol 2004;64(2):239–44.
[8] Durville D. Simulation of the mechanical behaviour of woven fabrics at the scale of fibers. Int J Mater Form 2010;3(S2):1241–51.
[9] Latil P, Orgéas L, Geindreau C, Dumont PJJ, du Roscoat SR. Towards the 3D in situ characterisation of deformation micro-mechanisms within a compressed bundle of fibres. Compos Sci Technol 2011;71(4):480–8.
[10] Tang XD, Whitcomb JD. General techniques for exploiting periodicity and symmetries in micromechanics analysis of textile composites. J Compos Mater 2003;37(13):1167–89.
[11] Miehe C, Dettmar J. A framework for micro–macro transitions in periodic particle aggregates of granular materials. Comput Methods Appl Mech Eng 2004;193(3):225–56.
[12] Lomov SV, Ivanov DS, Verpoest I, Zako M, Kurashiki T, Nakai H, et al. Meso-FE modelling of textile composites: road map and data flow and algorithms. Compos Sci Technol 2007;67(9):1870–91.
[13] Badel P, Vidal-Sallé E, Boisse P. Computational determination of in-plane shear mechanical behaviour of textile composite reinforcements. Comput Mater Sci 2007;40(4):439–48.
[14] Tabatabaei SA, Lomov SV, Verpoest I. Assessment of embedded element technique in meso-FE modelling of fibre reinforced composites. Compos Struct 2014;107:436–46.
[15] Pickett AK, Fouinneteau MRC. Material characterisation and calibration of a meso-mechanical damage model for braid reinforced composites. Compos A: Appl Sci Manuf 2006;37(2):368–77.
[16] Bickerton S, Simacek P, Guglielmi SE, Advani SG. Investigation of draping and its effects on the mold filling process during manufacturing of a compound curved composite part. Compos A: Appl Sci Manuf 1997;28(9–10):801–16.
[17] Loix F, Badel P, Orgeas L, Geindreau C, Boisse P. Woven fabric permeability: from textile deformation to fluid flow mesoscale simulations. Compos Sci Technol 2008;68(7–8):1624–30.
[18] Mahdi S, Gama BA, Yarlagadda S, Gillespie Jr JW. Effect of the manufacturing process on the interfacial properties and structural performance of multi-functional composite structures. Compos A: Appl Sci Manuf 2003;34(7):635–47.
[19] Long AC, Brown LP. Modelling the geometry of textile reinforcements for composites: TexGen. In: Boisse P, editor. Composite reinforcements for optimum performance. Woodhead Publishing; 2011. p. 239–64.
[20] Lomov SV. Modelling the geometry of textile reinforcements for composites: WiseTex. In: Boisse P, editor. Composite reinforcements for optimum performance. Woodhead Publishing; 2011. p. 200–38.
[21] De Luycker E, Morestin F, Boisse P, Marsal D. Simulation of 3D interlock composite preforming. Compos Struct 2009;88(4):615–23.
[22] Green SD, Long AC, Said BSFE, Hallett SR. Numerical modelling of 3D woven preform deformations. Compos Struct 2014;108:747–56.
[23] Baruchel J, Buffiere J, Maire E, Merle P, Peix G. In: Baruchel J, Buffiere J, Maire E, Merle P, Peix G, editors. X-ray tomography in material science. Hermes Science; 2000.
[24] Desplentere F, Lomov SV, Woerdeman DL, Verpoest I, Wevers M, Bogdanovich A. Micro-CT characterization of variability in 3D textile architecture. Compos Sci Technol 2005;65(13):1920–30.
[25] Hsieh J. In: Hsieh J, editor. Computed tomography: principles, design, artifacts, and recent advances. SPIE Press; 2009.
[26] Herman GT. In: Herman GT, editor. Image reconstruction from projections: the fundamentals of computerized tomography. New York: Academic Press; 1980.
[27] Khan AH, Chaudhuri RA. Fan-beam geometry based inversion algorithm in computed tomography (CT) for imaging of composite materials. Compos Struct 2014;110:297–304.
[28] Boisse P, Gasser A, Hagège B, Billoet JL. Analysis of the mechanical behavior of woven fibrous material using virtual tests at the unit cell level. J Mater Sci 2005;40(22):5955–62.
[29] Badel P, Vidal-Sallé E, Boisse P. Large deformation analysis of fibrous materials using rate constitutive equations. Comput Struct 2008;86:1164–75.
[30] Bigun J, Bigun T, Nilsson K. Recognition by symmetry derivatives and the generalized structure tensor. IEEE Trans Pattern Anal Mach Intell 2004;26(12):1590–605.
[31] Jahne B. In: Jahne B, editor. Spatio-temporal image processing: theory and scientific applications. Springer; 1993.
[32] Rezakhaniha R, Agianniotis A, Schrauwen JTC, Griffa A, Sage D, Bouten CVC, et al. Experimental investigation of collagen waviness and orientation in the arterial adventitia using confocal laser scanning microscopy. Biomech Model Mechanobiol 2011;11(3–4):461–73.
[33] Jeulin D, Moreaud M. Segmentation of 2D and 3D textures from estimates of the local orientation. Image Anal Stereol 2008;27:183–92.
[34] Borgefors G, Nystrom I, Sanniti di Baja G. Computing skeletons in three dimensions. Pattern Recogn 1999;32(7):1225–36.
[35] Fouard C, Malandain G, Prohaska S, Westerhoff M. Blockwise processing applied to brain microvascular network study. IEEE Trans Med Imaging 2006;25:1319–28.
[36] Palagyi K, Balogh E, Kuba A, Halmai C, Erdohelyi B, Sorantin E, et al. A sequential 3D thinning algorithm and its medical applications. In: Insana M, Leahy R, editors. Lecture notes in computer science. Berlin Heidelberg: Springer; 2001. p. 409–15.
[37] Tsao Y, Fu K. A parallel thinning algorithm for 3-D pictures. Comput Graphics Image Process 1981;17:315–31.

[38] Gong W, Bertrand G. A simple parallel 3D thinning algorithm. In: 10th International conference on pattern recognition. Atlantic City, NJ; 1990. p. 188–90.
[39] Jonker P. Morphological operations on 3D and 4D images: from shape primitive detection to skeletonization. In: Borgefors G, Nystrom I, Baja G, editors. Lecture notes in computer science [internet]. Berlin Heidelberg: Springer; 2000. p. 371–91.
[40] Calabi L, Harnett W. Shape recognition, prairie fires, convex deficiences and skeletons. Am Math Mon 1968;75(4):335–42.
[41] Zhou Y, Kaufman A, Toga A. 3D skeleton and centerline generation based on an approximate minimum distance field. Int J Visual Comput 1998;14:303–14.
[42] Pudney C. Distance-ordered homotopic thinning: a skeletonization algorithm for 3D digital images. Comput Vision Image Understanding 1998;72:404–13.
[43] Frey PJ, George PL. In: Frey PJ, George PL, editors. Mesh generation. John Wiley & Sons; 2010.
[44] Lorensen WE, Cline HE. Marching cubes: a high resolution 3D surface construction algorithm. Proceedings of the 14th annual conference on Computer graphics and interactive techniques. New York, NY, USA: ACM; 1987. p. 163–9.
[45] Garland M, Heckbert PS. Surface simplification using quadric error metrics. Proceedings of the 24th annual conference on computer graphics and interactive techniques. New York, NY, USA: ACM Press/Addison-Wesley Publishing Co.; 1997. p. 209–16.
[46] Jin H, Tanner R. Generation of unstructured tetrahedral meshes by advancing front technique. Int J Numer Methods Eng 1993;36(11):1805–23.
[47] Löhner R, Parikh P. Generation of three-dimensional unstructured grids by the advancing-front method. Int J Numer Methods Fluids 1988;8(10):1135–49.
[48] Badel P, Vidal-Salle E, Maire E, Boisse P. Simulation and tomography analysis of textile composite reinforcement deformation at the mesoscopic scale. Compos Sci Technol 2008;68(12):2433–40.
[49] Potluri P, Parlak I, Ramgulam R, Sagar TV. Analysis of tow deformations in textile preforms subjected to forming forces. Compos Sci Technol 2006;66(2):297–305.
[50] Hypo-Elasticity Truesdell C. Indiana Univ Math J 1955;4(1):83–133.
[51] Xiao H, Bruhns OT, Meyers A. On objective corotational rates and their defining spin tensors. Int J Solids Struct 1998;35(30):4001–14.
[52] Hughes TJR, Winget J. Finite rotation effects in numerical integration of rate constitutive equations arising in large-deformation analysis. Int J Numer Methods Eng 1980;15(12):1862–7.
[53] Dienes JK. On the analysis of rotation and stress rate in deforming bodies. Acta Mech 1979;32(4):217–32.
[54] Dafalias Y. Corotational rates for kinematic hardening at large plastic deformations. J Appl Mech 1983;50(3):561–5.
[55] Gasser A, Boisse P, Hanklar S. Mechanical behaviour of dry fabric reinforcements. 3D simulations versus biaxial tests. Comput Mater Sci 2000;17(1):7–20.
[56] Cornelissen B, Sachs U, Rietman B, Akkerman R. Dry friction characterisation of carbon fibre tow and satin weave fabric for composite applications. Compos A: Appl Sci Manuf 2014;56:127–35.
[57] Cornelissen B, Rietman B, Akkerman R. Frictional behaviour of high performance fibrous tows: friction experiments. Compos A: Appl Sci Manuf 2013;44:95–104.
[58] Gorczyca-Cole JL, Sherwood JA, Chen J. A friction model for thermostamping commingled glass–polypropylene woven fabrics. Compos A: Appl Sci Manuf 2007;38(2):393–406.
[59] Potluri P, Thammandra VS. Influence of uniaxial and biaxial tension on meso-scale geometry and strain fields in a woven composite. Compos Struct 2007;77(3):405–18.
[60] Schnur DS, Zabaras N. An inverse method for determining elastic material properties and a material interface. Int J Numer Methods Eng 1992;33(10):2039–57.
[61] Kelly P. Transverse compression properties of composite reinforcements. Composite reinforcements for optimum performance. Woodhead Publishing; 2011. p. 333–66.
[62] Nguyen QT, Vidal-Salle E, Boisse P, Park CH, Saouab A, Breard J, et al. Mesoscopic scale analyses of textile composite reinforcement compaction. Compos B: Eng 2013;44(1):231–41.
[63] Robitaille F, Long A, Jones IA, Rudd CD. Automatically generated geometric descriptions of textile and composite unit cells. Compos A: Appl Sci Manuf 2003;34(4):303–12.
[64] Smitheman SA, Fontana Q, Davies MG, Li S, Jones IA, Long AC, Ruijter W. Unit cell modelling and experimental measurement of the elastic and thermoelastic properties of sheared textile composites. In: Proceedings of the 10th international conference on textile composites (TexComp 10). Lille, France; 2010.
[65] <http://texgen.sourceforge.net/index.php/Main_Page>.